

Geometric Phase Atom Optics and Interferometry

B. Zygelman*

Department of Physics and Astronomy, University of Nevada, Las Vegas, Las Vegas NV 89154

(Dated: October 25, 2018)

We illustrate how geometric gauge forces and topological phase effects emerge in atomic and molecular systems without employing assumptions that rely on adiabaticity. We show how geometric magnetism may be harnessed to engineer novel quantum devices including a velocity sieve, a component in mass spectrometers, for neutral atoms. We introduce and outline a possible experimental setup that demonstrates topological interferometry for neutral spin 1/2 systems. For that 2-level system, we study the transition from Abelian to non-Abelian behavior and explore its relation to the molecular Aharonov-Bohm (MAB) effect.

I. INTRODUCTION

Berry's phase[1], a realization of a non-integrable phase factor[2, 3], plays an important role in describing adiabatic quantum evolution in a semi-classical setting. It is also known[4–8] that effective gauge potentials, that give rise to such phases, emerge in fully quantal systems in which true adiabaticity is ill-defined. In addition to generating phase holonomies[4], they may lead to effective Lorentz-like forces[6, 8, 9] acting on the quantum system.

Today, applications of geometric gauge forces in cold many-body systems[10, 11] is an active and topical area of research. Dressing atoms using lasers[12], researchers[13, 14] have been able to engineer Lorentz-like forces, an effect sometimes called geometric[9, 15], synthetic[11] or artificial magnetism[10], in ensembles of cold atoms. It is hoped that the latter may allow realization of novel quantum Hall physics in a quantum degenerate gas.

Another possible application of geometric magnetism is in the manipulation of individual neutral atoms or neutrons[15–17]. In Refs. [15, 16] we proposed how gauge forces could be exploited to construct “magnetic lenses” for neutral matter. In this paper we elaborate on those observations by introducing two novel and striking illustrations of the latter. In the first example we illustrate how this phenomenon allows realization of a velocity sieve, a component in mass spectrometers, for beams of neutral particles. In another example we consider a quantum mechanical analog[15, 18, 19] of a field theoretical model[18] to demonstrate topological quantum interferometry for neutral spin-1/2 systems. Its laboratory realization could have applications in topological quantum computing protocols.

With some exceptions e.g. [15, 17, 20], most theoretical studies, by necessity, have relied on some form of the adiabatic assumption, i.e. the Born-Oppenheimer (BO) approximation. Gauge potentials are explicit in the adiabatic picture but it is also known[21, 22] that those effective (non-Abelian) gauge potentials describe a pure gauge[3].

Consider the following Schroedinger equations

$$-\frac{\hbar^2}{2m}\nabla_{\mathbf{R}}^2\psi + V(\mathbf{R})\psi = i\hbar\frac{\partial\psi}{\partial t} \quad (1)$$

and

$$-\frac{\hbar^2}{2m}(\nabla_{\mathbf{R}} - i\mathbf{A})^2\psi' + V(\mathbf{R})\psi' = i\hbar\frac{\partial\psi'}{\partial t} \quad (2)$$

for amplitudes ψ , ψ' respectively. We take them to be n dimensional column vectors and $V(\mathbf{R})$ is a local $n \times n$ matrix potential. The gauge potential

$$\mathbf{A} \equiv iU^\dagger(\mathbf{R})\nabla_{\mathbf{R}}U(\mathbf{R}) \quad (3)$$

where $U(\mathbf{R})$ is a differentiable, single-valued, unitary $n \times n$ matrix. According to definition (3) \mathbf{A} is a pure gauge [3, 21]. We pose the question; do the Schroedinger equations (1) and (2) describe the same physics? If $n = 1$ the answer is in the affirmative since then $U(\mathbf{R}) = \exp(-i\Omega)$ and

$$\mathbf{A} \equiv i\exp(i\Omega)\nabla_{\mathbf{R}}\exp(-i\Omega) = \nabla_{\mathbf{R}}\Omega \quad (4)$$

where Ω is a single-valued function of \mathbf{R} . Therefore, $\psi' = \exp(i\Omega)\psi$ and the physical content of Eqs (1) and (2) are identical[23], as the eigenvalues of physical operators, which transform in a covariant manner, are invariant under this gauge transformation. The same is true for the non-Abelian case where $n > 1$, provided that $[U, V] = 0$ since then $\psi' = U(\mathbf{R})\psi$. So for these cases we find that the minimal coupling of a pure gauge potential is fully equivalent to a description where $\mathbf{A} = 0$. However this is not the case if $[\mathbf{A}, V] \neq 0$, as the amplitudes ψ , and ψ' are no longer related by the (single-valued) gauge transformation U . The conclusion follows from the fact that $[U(\mathbf{R}), V] \neq 0$ if the above inequality holds (see also Appendix C). The implications of this observation will become apparent in the discussion below.

Are non-trivial gauge forces an artifact of the adiabatic approximation[20]? Are singularities in the adiabatic Hamiltonian solely responsible for the emergence of topological phases? Several interpretations[24–26] for the origins of geometric gauge forces have been advanced. However, compelling examples that offer fully quantum solutions to systems in which such forces arise in the

* bernard@physics.unlv.edu

adiabatic limit have largely been unavailable and, therefore, predictions are limited by the validity of assumptions based on adiabaticity.

In order to address questions and deficiencies in theoretical approaches that assume adiabaticity, we [15, 16] introduced a wave packet propagation scheme that does not require the assumptions and restrictions imposed by it. The resulting time dependent solutions for the systems are exact, within the bounds imposed by numerical error, and they are not compromised by issues relating to the robustness of the adiabatic approximation. This allows us to make definitive verdicts on the fidelity of predictions informed by the latter, and the gauge theory interpretation that follows from it.

In the discussion below we first present the general theoretical framework for the specific cases considered. We introduce a 2-level system whose adiabatic Hamiltonian is defined in such a way that there is a cancellation of the effective Lorentz force with the gradient force in low energy solutions to the coupled Schroedinger equation. This cancellation is similar to that which occurs when appropriate external electric and magnetic fields “select” the velocity of a charged particle beam. This theoretical model illustrates how geometric magnetism could be harnessed to entertain similar capabilities for neutral systems. We then focus our discussion on neutral spin-1/2 systems subjected to an external magnetic field. We show, with the appropriate external field configuration, how such a system can exhibit topological Aharonov-Bohm[27] (AB) behavior. Though it has been discussed previously[15, 18, 19] within the framework of the BO approximation, here we offer fully time dependent, coupled channel, wave packet solutions without employing assumptions based on adiabaticity. This capability allows us extend the analysis to cases in which the BO approximation is no longer valid. We investigate how this systems transitions at low energies, and one that allows an Abelian description in which the AB gauge vector potential emerges, to that in which non-Abelian features arise. Finally, we explore the relationship of this system to a phenomenon that occurs in molecular systems that possess conical intersections[4, 20, 28, 29]. Atomic units will be used throughout, unless otherwise indicated.

II. THEORY

A. Velocity sieve

Consider the model Hamiltonian for an atom, or n-state, system

$$H = -\frac{\hbar^2}{2m}\nabla_{\mathbf{R}}^2 + H_{ad}(\mathbf{R}). \quad (5)$$

\mathbf{R} is the position operator for the atom and $H_{ad}(\mathbf{R})$ is the adiabatic Hamiltonian that generates its internal dynamics. Suppose it can be decomposed into the form

$U(\mathbf{R})H_{BO}U^\dagger(\mathbf{R})$, where $H_{BO}(\mathbf{R})$ is an n-dimensional diagonal matrix with eigenvalues $\epsilon_i(\mathbf{R})$, and $U(\mathbf{R})$ is a unitary matrix. In this discussion we consider the case where $n = 2$, and $\mathbf{R} = (x, y)$ and limit $H_{ad}(\mathbf{R})$ to be time independent. We require $U(\mathbf{R})$ to be single-valued[30] and express it

$$U = \exp(-i\sigma_3\phi/2)\exp(-i\sigma_2\Omega/2)\exp(i\sigma_3\phi/2) \quad (6)$$

where σ_i are the Pauli matrices, and ϕ, Ω are single-valued functions of the planar coordinates (x, y) .

We choose, as in Ref. [15],

$$\begin{aligned} \Omega(x, y) &= \frac{\pi}{2}(1 + \tanh(\beta x)) \\ \phi(x, y) &= LB_0 y \end{aligned} \quad (7)$$

where L, B_0, β are constants.

In solving the Schroedinger equation $i\hbar\partial\psi/\partial t = H\psi$ it is useful to expand ψ in the basis of the adiabatic eigenstates of H_{ad} . In that description we arrive at the set of coupled, Schroedinger-like, equations for the multi-channel amplitudes that are minimally coupled to a pure, non-Abelian, gauge potential $\mathbf{A}(\mathbf{R}) \equiv iU^\dagger(\mathbf{R})\nabla U(\mathbf{R})$, as well as the diagonal scalar potential matrix H_{BO} whose entries are labeled by $\epsilon_i(\mathbf{R})$ and correspond to the Born-Oppenheimer energies of H_{ad} . We now invoke the Born-Oppenheimer (BO) approximation and project these coupled equations unto, open, ground-state BO amplitude $F(\mathbf{R})$. We get,

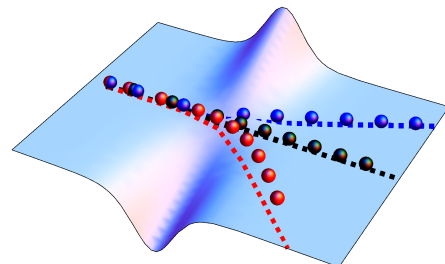


FIG. 1: (Color online) Classical trajectories (dotted lines) obtained from solutions to Eq. (12) for various initial velocities. Colored spheres correspond to, time lapse, expectation values obtained from solutions of the coupled channel quantum mechanical problem generated by Hamiltonian Eq.(5). The black spheres pass undeflected with their initial velocities.

$$\begin{aligned} -\frac{\hbar^2}{2m}\left(\nabla - i\mathbf{A}_P\right)^2 F(\mathbf{R}) + \tilde{V}_{BO}(\mathbf{R})F(\mathbf{R}) &= EF(\mathbf{R}). \\ \tilde{V}_{BO}(\mathbf{R}) &= \epsilon_2(\mathbf{R}) + b(\mathbf{R}) \\ b(\mathbf{R}) &\equiv \frac{\hbar^2}{2m}\mathbf{A}_{12} \cdot \mathbf{A}_{12} \end{aligned} \quad (8)$$

where $b(\mathbf{R})$ [6, 31] is related, but not equivalent, to the adiabatic[32] or Born-Huang correction[33]. Typically the BO approximation is justified[33] if, for total (collision) energy E , the inequalities $\epsilon_1(\mathbf{R}) \gg E > \epsilon_2(\mathbf{R})$, $\Delta\epsilon \equiv \epsilon_1 - \epsilon_2 \gg b(\mathbf{R})$ are satisfied. \mathbf{A}_P is a vector potential and is obtained by projecting the non-Abelian gauge potential so that $\mathbf{A}_P = \text{Tr} P \mathbf{A} P$ $P \equiv |g\rangle\langle g|$, where $|g\rangle$ is the ground eigenstate of H_{BO} with eigenvalue $\epsilon_2(\mathbf{R})$, and \mathbf{A}_{12} is the off-diagonal component of \mathbf{A} . With this parameterization we obtain, for the ground adiabatic state, an effective curvature

$$\mathbf{H} = \nabla \times \hbar \mathbf{A}_P = \hat{\mathbf{k}} \frac{\hbar}{4} \pi B_0 L \beta \text{sech}^2(\beta x) \cos\left(\frac{\pi}{2} \tan h(\beta x)\right). \quad (9)$$

Though \mathbf{A} describes a pure non-Abelian gauge and so has vanishing curvature, \mathbf{A}_P may have a non-trivial curvature, which for a non-degenerate ground state discussed here has the Abelian form $\mathbf{H} \equiv \nabla \times \mathbf{A}_P$.

The classical limit for Eq. (8) corresponds to a situation in which the motion of the atom is governed by[6]

$$m \frac{d^2 \mathbf{R}(t)}{dt^2} = \mathbf{v} \times \mathbf{H} - \nabla \tilde{V}_{BO} \quad (10)$$

where $\mathbf{R}(t)$ is the atom position coordinate.

In addition to the conventional scalar gradient force $-\nabla \tilde{V}_{BO}(\mathbf{R})$, (sometimes called the Hellmann-Feynman force), the atom experiences an effective velocity dependent Lorentz force. We argued[15, 16] that such forces could be exploited to construct effective ‘‘magnetic lenses’’ for neutral atoms or neutrons. Here we underscore that observation by demonstrating that both the induced scalar and vector forces could be used in conjunction to develop novel capabilities for the manipulation and control of neutral particle beams. In particular, we describe a neutral particle velocity sieve that exploits both the velocity dependent force arising from geometric magnetism as well as the Hellmann-Feynman force.

It is well known that for charged particles a velocity selector can be realized by choosing a suitable geometry in which a uniform magnetic field, \mathbf{H} , induces a Lorentz force that cancels the gradient force produced by an electric field, \mathbf{E} , so that for a particle of charge q and velocity v , $vqH = qE$. Pursuing this analogy we construct a Hamiltonian of the form given in Eq. (5) where the entries of the BO eigenenergies are given by,

$$H_{BO} = \sigma_3 (\epsilon(\mathbf{R}) + \Delta) - b(\mathbf{R}) \\ \epsilon(\mathbf{R}) = v_0 y H(x) \quad H(x) \equiv |\mathbf{H}| \quad (11)$$

and where Δ is chosen to be a sufficiently large energy gap so that the BO projection approximation into the ground state is justified. In definition Eq. (11) we have included a counter-term $b(\mathbf{R})$ defined in Eq.(8). In the BO approximation its presence cancels the adiabatic correction generated by the off-diagonal components of \mathbf{A} . With this choice, Eq. (10) becomes

$$m \frac{d^2 x}{dt^2} = \frac{dy}{dt} H(x(t)) + y(t) v_0 \partial_x H(x(t))$$

$$m \frac{d^2 y}{dt^2} = -\frac{dx}{dt} H(x(t)) + v_0 H(x(t)). \quad (12)$$

In the asymptotic region $x \rightarrow -\infty$ all forces vanish and if we take the initial condition $\dot{y} = 0, \dot{x} = v_0$, $x(t) = v_0 t + x_0, y(t) = 0$ is a solution to Eqs. (12). For other impact parameters and velocities numerical solution of Eq. (12) predict trajectories in which the incoming particle is scattered. This behavior is illustrated in Figure (1) where dashed lines represent classical trajectories superimposed on the BO potential surface (ignoring the energy gap Δ). The black line represents the solution in which an atom with initial velocity v_0 propagates at constant velocity unimpeded. The blue and red lines correspond to initial velocities slightly larger and smaller, respectively, than v_0 . Atoms with these velocities are clearly scattered by the effective Lorentz and gradient forces.

Below we demonstrate that this behavior is shared with quantum evolution generated by Hamiltonian (5). The atom is initially in its ground state in the asymptotic region and we propagate its amplitude using the time dependent method given in Refs.[15, 16]. The packets are described by

$$\psi \equiv \begin{pmatrix} f \\ g \end{pmatrix}$$

whose components obey the coupled Schroedinger equations

$$i\hbar \frac{\partial f}{\partial t} = -\frac{\hbar^2}{2m} \nabla^2 f + (V - b(\mathbf{R})) f + V_{12} g \\ i\hbar \frac{\partial g}{\partial t} = -\frac{\hbar^2}{2m} \nabla^2 g + V_{12}^* f - (V + b(\mathbf{R})) g \quad (13)$$

where

$$V = (\Delta + \epsilon(\mathbf{R})) \cos(\Omega(x)) \\ V_{12} = \exp(-i\phi(y)) (\Delta + \epsilon(\mathbf{R})) \sin(\Omega(x)). \quad (14)$$

In the remote past the packets have initial starting positions outside the interaction region with null impact parameters. In Figure (1) the black spheres represent propagation of packets with initial velocity v_0 . The centers of the packets track closely the classical trajectory. The blue and red spheres have initial velocities slightly greater and smaller, respectively, than v_0 . The quantum simulation illustrated in that figure clearly demonstrates the proposed velocity selection effect for this system. Though Hamiltonian (5) is a simple, time independent, two-state (or qubit) system, its experimental realization may pose challenges. Below we introduce another, more familiar, two-state system a neutral spin 1/2 system (eg. atom, neutron) subjected to a static external magnetic field. In the geometry discussed below we show how geometric phase induced, Aharonov-Bohm like, interferometry can be realized by it.

B. Geometric phase, Aharonov-Bohm, interferometry



FIG. 2: (Color online) Time lapse illustration of a pair of coherent Gaussian wave packets initially in the ground state. At $\tau = 0$ the pair of coherent packets are shown in the upper right and left sides of the figure. At a later time, the packets coalesce thus creating the interference pattern.

Consider the external magnetic field

$$\mathbf{B} = B(\rho) \hat{\phi} + B_0 \hat{\mathbf{k}} \quad (15)$$

where ϕ, ρ are the polar and radial coordinates in a cylindrical coordinate system, and B_0 is a constant, and we ignore motion in the z directions as it can be factored from the planar motion. If $B(\rho) = \lambda/\rho$ then Eq. (15) describes the field generated by a wire with current along the z -axis superimposed with that of a homogeneous magnetic field $B_0 \hat{\mathbf{k}}$. The Hamiltonian of a neutral spin-1/2 atom is then given by

$$H = -\frac{\hbar^2}{2m} \nabla^2 + \mu_B \boldsymbol{\sigma} \cdot \mathbf{B} \quad (16)$$

(alternatively, for a neutron μ_B is replaced by its magnetic moment). We can re-express the internal Hamiltonian $H_{ad} = \mu_B \boldsymbol{\sigma} \cdot \mathbf{B}$ as

$$H_{ad} = \mu_B \begin{pmatrix} B_0 & -i \exp(-i\phi)B(\rho) \\ i \exp(i\phi)B(\rho) & -B_0 \end{pmatrix} = U H_{BO} U^\dagger \quad (17)$$

where

$$H_{BO} = \mu_B \begin{pmatrix} \sqrt{B_0^2 + B^2(\rho)} & 0 \\ 0 & -\sqrt{B_0^2 + B^2(\rho)} \end{pmatrix} \quad (18)$$

and

$$U = \exp(-i\sigma_3\phi/2) \exp(i\sigma_1\Omega(\rho)/2) \exp(i\sigma_3\phi/2) \quad (19)$$

with ϕ, ρ , the azimuthal angle and radial distance, in a cylindrical coordinate system, respectively and $\tan(\Omega) = B(\rho)/B_0$. Thus,

$$\mathbf{A}(\mathbf{R}) \equiv iU^\dagger(\mathbf{R}) \nabla U(\mathbf{R}) = \hat{\phi} A_\phi + \hat{\rho} A_\rho$$

$$A_\phi = \frac{1}{2\rho} \begin{pmatrix} \cos \Omega(\rho) - 1 & ie^{-i\phi} \sin \Omega(\rho) \\ -ie^{i\phi} \sin \Omega(\rho) & 1 - \cos \Omega(\rho) \end{pmatrix}$$

$$A_\rho = -\frac{\Omega'(\rho)}{2} \begin{pmatrix} 0 & e^{-i\phi} \\ e^{i\phi} & 0 \end{pmatrix} \quad (20)$$

and so,

$$\mathbf{A}_P = \text{Tr } P \mathbf{A} P = \frac{1 - \cos \Omega(\rho)}{2\rho}$$

$$\tilde{V}_{BO} = -\mu_B \sqrt{B_0^2 + B^2(\rho)} + b(\rho)$$

$$b(\rho) = \frac{\hbar^2}{2m} \left(\frac{\sin^2 \Omega(\rho)/2}{\rho^2} + \frac{\Omega'(\rho)}{4} \right). \quad (21)$$

The effective curvature for the ground adiabatic state is,

$$\mathbf{H} \equiv \nabla \times \hbar \mathbf{A}_P = \hat{\mathbf{k}} \frac{\hbar}{2\rho} \sin(\Omega(\rho)) \Omega'(\rho). \quad (22)$$

The above analysis is relevant in studies of the motion of cold atoms, that have a magnetic dipole moment, in the vicinity of current carrying wire (or nanotube)[34]. Here we focus on a special case, that in which $B(\rho)$ is a constant B_ρ . For this case, according to Eq. (22), $\mathbf{H} = 0$, and because $V_{BO}(\rho)$ is also constant, and ignoring $b(\rho)$ (which is very small in the region $\rho \neq 0$ traversed by the packets), the atom does not experience either a velocity dependent Lorentz, or scalar force. However, the induced vector potential \mathbf{A}_P is not trivial and is given by

$$\mathbf{A}_P = \hat{\phi} \frac{\Phi}{2\pi\rho}, \quad (23)$$

where

$$\Phi = \pi(1 - \cos \Omega) = \pi \left(1 - \frac{B_0}{\sqrt{B_0^2 + B_\rho^2}} \right). \quad (24)$$

Packet propagation is again described as in Eq. (13) but now

$$V = \mu_B B_0$$

$$V_{12} = -i \mu_B \exp(-i\phi) B_\rho. \quad (25)$$

In order to demonstrate the proposed thesis we propagate two identical, coherent wave packets as shown in Figure 2. The packets are displaced from the origin and are allowed to propagate, having been given initial velocities that allow them to coalesce, at time τ_c , and form the interference pattern shown in that figure. In our simulation we have first set $B_\rho = 0$ so that the packets propagate freely. In that case the horizontal line that passes through the center where the two packets meet, the wave function has the analytic form (see Appendix A)

$$\frac{8a^2 k^2 \exp\left(-\frac{2a^2 k^2 \eta^2}{4a^4 k^2 + \eta_0^2}\right)}{4a^4 k^2 \pi + \pi \eta_0^2} \cos^2(k\eta) \quad (26)$$

where η is the horizontal coordinate, k is a scaled wavenumber, η_0 are the initial displacements of the packets from the origin and a is the initial width of each

packet. This function is plotted by the red line in Figure (3). In panel (a) of that figure we superimpose the values, shown by the blue circles, obtained in our numerical simulation. We find excellent agreement with the analytic result Eq. (26) and validates the numerical procedure used in this study. In panel (b) we plot the correspond interference pattern when B_0, B_ρ has the value so that $\Omega = \pi/2$. We notice a distinct shift in the calculated interference pattern from that given by Eq. (26). However, a fit with the replacement in Eq. (26)

$$\cos^2(k\eta) \rightarrow \cos^2(k\eta + \Phi/4) \quad (27)$$

provides an excellent approximation to the calculated

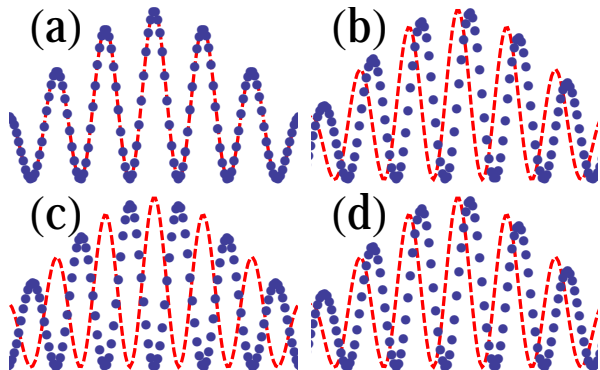


FIG. 3: (Color online) (a) Cross section of the interference pattern shown in Figure (2). Red dashed line represents the analytic form Eq. (26). Blue dots represent results from numerical solution for the case $\Omega = 0$. (b) Blue dots represent interference cross section for the case $\Omega = \pi/2$. (c) Same as above for $\Omega = \pi$, (d) Same as above for $\Omega = 3\pi/2$.

data given by the simulation.

We now consider the propagation of the two initial packets, at $t = 0$, having their vertical velocities reversed so that they propagate into the upper half plane and coalesce at a point that is the reflection of the coalescence point shown in Figure (2). The resulting interference pattern is illustrated in Figure (4). At the point d the pattern is again well described by Eq. (26) but with the replacement

$$\cos^2(k\eta) \rightarrow \cos^2(k\eta - \Phi/4) \quad (28)$$

Because Hamiltonian (16) is not invariant under reflection about the η (horizontal) axis it is not surprising that the interference pattern at point d differs from that at point b . It might not be as obvious that the difference is topological in nature. According to the discussion above the locations on the η axis where local minima occur is given by

$$\eta_m = \frac{m\pi}{2k} \pm \frac{\Phi}{4k} \quad (29)$$

where the \pm sign identifies the points on the horizontal lines passing through the points b and d respectively and

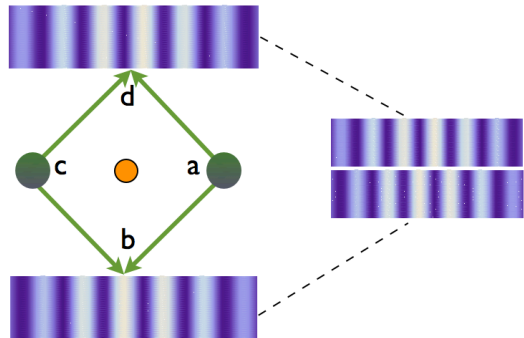


FIG. 4: (Color online) Fringe shifts produced by wave packet propagation of ground state solutions for the Hamiltonian given in Eq. (16)

m is an integer. Therefore there is a displacement

$$\Delta\eta_m = \frac{\Phi}{2k} \quad (30)$$

shown by the right hand panel of Figure (4), in the location of the relative minima between the upper and lower fringe patterns. It depends on the quantity Φ , which according to AB theory is given by

$$\int_C d\mathbf{r} \cdot \mathbf{A}_{AB} \quad (31)$$

where C is a contour that encircles the path $adcb$ in Figure(4) and \mathbf{A}_{AB} is given by Eq.(23). The connection with AB theory, and the topological nature of the fringe shift, becomes evident when we shift the packet paths, so that a displaced closed circuit $a'd'c'b'a'$ no longer includes the fictitious flux tube located at the origin. In that case our simulations show that the difference in the fringes at the corresponding locations of b', d' disappear, in harmony with the predictions of the gauge theory analysis.

In the discussion above we presented the full quantum mechanical simulation of coupled equations (13) in order to derive the fringe patterns discussed above. However, in order to gain additional insight it is useful to appeal to semiclassical analysis of this system. Below we show how the results discussed above can be re-derived using a semiclassical framework in the adiabatic representation of Eqs. (13).

C. Semi-classical description of packet propagation in an Abelian gauge potential

Consider the wave packet $\psi_1(\xi, \eta, \tau)$ defined by Eq. (A1) and whose center, at $\tau = 0$, is located at point a in Figure (4). We need to predict the packet that grows out of it and whose evolution is determined by the coupled

Schroedinger Eq.(13). Our calculation show that, under the adiabatic condition $\Delta/k^2 \gg 1$, $\Delta \equiv \mu_B \sqrt{B_0^2 + B_\rho^2}$, and in the adiabatic gauge, a good approximation for it at the time its center arrives at b is

$$U(a, b)\psi_1(b) \quad (32)$$

where ψ_1 is the free particle packet and the unitary operator $U(a, b)$ is given by

$$U(a, b) \approx \exp(i \int_{C_1} d\mathbf{r} \cdot \mathbf{A}_P). \quad (33)$$

Here C_1 represent a path integral along segment $a-b$ that starts at a and ends at b and \mathbf{A}_P is the gauge potential given by expression (23).

Similarly, a packet initially centered at c at $\tau = 0$, translates along path $c-b$ and arrives at b at τ_c . It can be expressed

$$U(c, b)\psi_2(b) \quad (34)$$

where ψ_2 is defined in Eq. (A1). The coherent sum of these amplitudes at $\tau = \tau_c$ is then given by the expression

$$\begin{aligned} \psi(b) &= U(a, b)\psi_1(b) + U(c, b)\psi_2(b) = \\ &U(c, b)(U^{-1}(c, b)U(a, b)\psi_1(b) + \psi_2(b)) = \\ &U(c, b)(U(b, c)U(a, b)\psi_1(b) + \psi_2(b)) = \\ &U(c, b)(U(a, c)\psi_1 + \psi_2(b)) \end{aligned} \quad (35)$$

where we made use of the unitary property of U and the relation $U(a, c) = U(b, c)U(a, b)$. Therefore

$$|\psi(b)|^2 = |\psi_2(b) + U(a, c)\psi_1(b)|^2 \quad (36)$$

Evaluating

$$U(a, c) = \exp(i \int_{abc} d\mathbf{r} \cdot \mathbf{A}_P) = \exp(-i \frac{\Phi}{2}) \quad (37)$$

and inserting this into Eq. (35) we obtain expression Eq. (27).

We obtain an analogous relation for the case where the momenta, along the ξ direction, of the initial wave packets at a, c are reversed so that at time τ_c the packets meet at point d in Figure 4. Following the steps outlined above we find

$$|\psi'(d)|^2 = |\psi'_2(d) + U'(a, c)\psi'_1(d)|^2 \quad (38)$$

where ψ'_i are the corresponding free-particle packets whose ξ momenta are reversed, and

$$U'(a, c) = \exp(i \int_{adc} d\mathbf{r} \cdot \mathbf{A}_P) = U_W U(a, c) \quad (39)$$

where U_W is a Wilson loop integral

$$U_W \equiv \exp(i \oint d\mathbf{r} \cdot \mathbf{A}_P) = \exp(i\Phi) \quad (40)$$

and the closed, counterclockwise, circuit encloses the origin.

According to Eq. (A4) $\psi'_i(\xi, \eta, \tau) = \psi_i(-\xi, \eta, \tau)$ and therefore,

$$|\psi'(d)|^2 = |\psi_2(b) + U_W U(a, c)\psi_1(b)|^2. \quad (41)$$

So the interference pattern $|\psi'(d)|^2$ at the top panel in Figure (4), differs from that at the lower panel by a, gauge invariant, phase determined by the Wilson loop U_W , in harmony with the results obtained by the, fully quantal, numerical simulation.

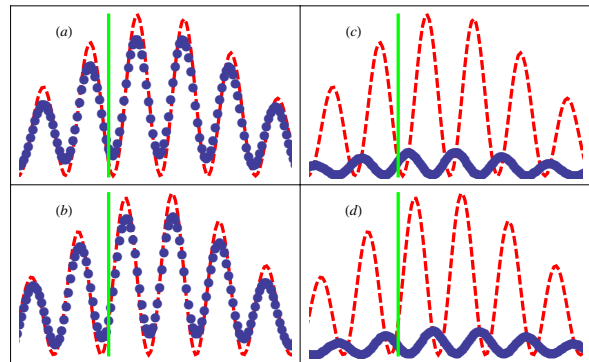


FIG. 5: (Color online) Interference fringes for energy defect $\Delta/k^2 = 0.1$ and $\Omega = 2\pi/3$. Panels (a),(b) are fringes (blue points) at locations b,d (bottom,top) in Figure (4) of text. Panels (c),(d) show fringes for (excited) state selected measurements at the latter locations. The green vertical line is a reference line to aid the eye in comparing fringes between the top and bottom panels. The dashed red lines correspond to fringes predicted by the Abelian semiclassical theory

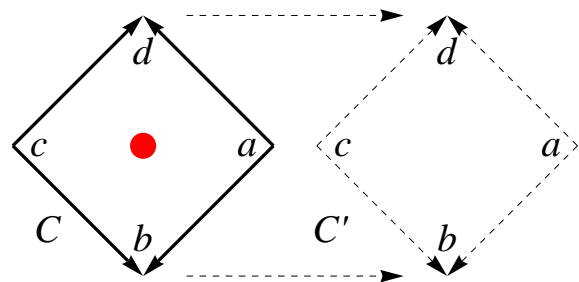


FIG. 6: (Color online) Circuit C which encloses fictitious flux tube (red disk), is translated to new circuit C' that does not enclose it.

D. Semi-classical description of packet propagation in a, pure, non-Abelian gauge potential

If the collision energy, $\frac{\hbar^2 k^2}{2m}$, is much larger than the energy defect 2Δ , between the Zeeman split spin states, non-adiabatic transitions between those states can occur. Thus if the initial localized wavepacket, say at point a

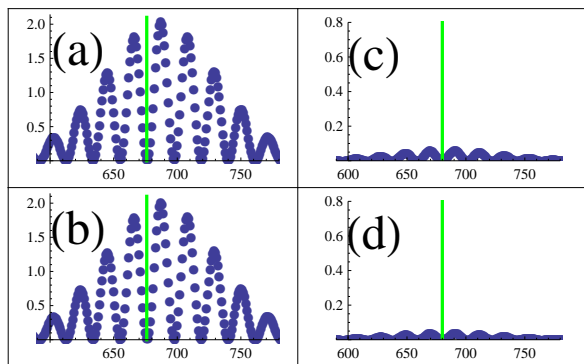


FIG. 7: (Color online) Interference fringes for energy defect $\Delta/k^2 = 0.1$ and $\Omega = 2\pi/3$ for loop diagram C' in Figure (6). Panels (a),(b) show fringes (blue points) at locations b,d (bottom,top) in Figure (6) respectively. Panels (c),(d) show fringes for (excited) state selected measurements at points b,d (bottom,top) in Figure (6) respectively. The green vertical line is a reference line to aid the eye in comparing fringes between the top and bottom panels.

in Figure (4), describes a particle in the ground Zeeman level, it will not necessarily stay in that level as the packet evolves in time.

In the discussion above we considered the adiabatic limit in which the ratio of energy defect to collision energy is large i.e. $\Delta/k^2 \gg 1$. In that limit spin flipping transitions between ground and excited Zeeman levels are suppressed. We showed that, in this limit, the single channel (or Abelian) Schrodinger equation (8) with gauge potential Eq. (23) and $V_{BO} = 0$ accurately predicts wavepacket dynamics and topological AB features. As the collision energy is cranked up so that $2\Delta/k^2 \leq 1$ we anticipate that the single channel (Abelian) description breaks down and non-Abelian features arise.

In Figure (5), panels (a), (b) we plot the interference patterns, corresponding to the top and bottom regions shown in Figure (4) for the collision energy corresponding to $\Delta/k^2 = 0.1$. Though the collision energy is sufficient to cause Zeeman level transitions, our results suggest that many of the Abelian features persist. First we note that there is a phase shift between the interference patterns, for the top and bottom regions respectively, that is nearly, but not exactly, predicted by the Abelian AB theory (which are shown in red in that figure). Panels (c),(d) show the fringes, for the top and bottom regions respectively for state-dependent probabilities, in this case for excitation into the upper Zeeman level. A distinct phase shift in the fringe patterns for excitation is also seen, though its structure is not predicted by the Abelian theory.

In order to investigate whether these features are topological we translate the loop C , shown in Figure (6), into the loop C' and repeat the calculations described above. Because loop C' does not enclose the fictitious flux tube

(shown by the red disk) classical AB theory suggests that the difference in fringe shifts, evident in Figure (5), is null. Indeed, this is the case. In panels (a),(b), of Figure (7), the probability interference are shown. The patterns for top and bottom regions (points d,b respectively) line up and no fringe shifts are evident. Panels (b),(d) of that figure show the corresponding interference patterns for the excited Zeeman level probabilities. Though fringe differences are negligible, we note a strong suppression of the latter (when compared to that for loop C shown in panels (b),(d) in Figure (5)). The suppression of excitation for loop C' is clearly a non-Abelian (or multichannel) feature.

Finally, we consider the extreme non-adiabatic regime. In it the ratio $\Delta/k^2 \rightarrow 0$ and we can again employ semiclassical methods[34] to predict the fringe patterns that are generated by our fully quantal simulations and which are shown below. In Figure (8) we repeat the calculations for propagation along loop C in Figure (6) for the values $\Delta/k^2 = 0.007$ and $\Omega = 2\pi/3$. Unlike the case for the adiabatic and near adiabatic regimes, in which topological fringe shifts arise, panels (a), (b) of Figure (8) clearly demonstrate absence of the topological fringe shift. This behavior can be explained using semiclassical methods. For, in that description[34] the total probability amplitude at point (b) in (4), that grows out of wave packet

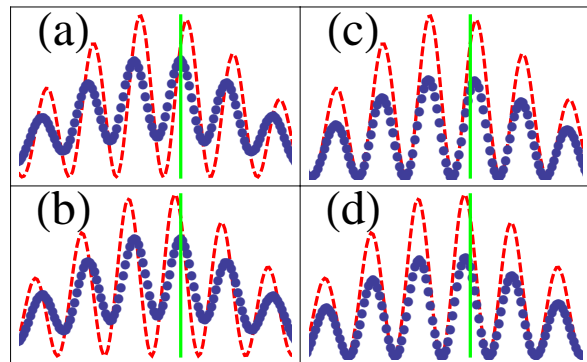


FIG. 8: (Color online) Interference fringes for energy defect $\Delta/k^2 = 0.007$ and $\Omega = 2\pi/3$. Panels (a,b) fringes (blue points) at locations b,d (bottom,top) in Figure (4) respectively. Panels (c,d) fringes for (ground) state selected measurements at points b,d (bottom,top) in Figure (4) respectively. The green vertical line is a reference line to aid the eye in comparing fringes between the top and bottom panels. The dashed red lines correspond to fringes predicted by the semiclassical Abelian theory

$\psi_1(a)$ is approximated by the expression

$$P \exp(i \int_{ab} d\mathbf{r} \cdot \mathbf{A}) \psi_1(b) \quad (42)$$

where P is a path-ordered integral, or Wilson line, along segment $a - b$, and \mathbf{A} is the non-Abelian, pure, gauge potential (20). Repeating the argument outlined above

for the fringe shift in the adiabatic limit, we now find that the shift depends on the Wilson loop integral

$$U_W \equiv P \exp(-i \oint dr \cdot \mathbf{A}) \quad (43)$$

where \mathbf{A} is given by Eq.(20). Because \mathbf{A} describes a pure gauge we find that $U_W = 1$ (see Appendix C) and so, unlike the case in the adiabatic regime, a fringe shift between the interference patterns at b, d in (4) does not manifest. Interestingly, this is no longer true if we perform state dependent measurements at locations b, d in that figure. In panels (c), (d) of Figure (8) we plot the calculated interference patterns at those points for a state selective measurement (in this case, the ground state). Those fringe shifts are, again, accurately predicted by the Abelian theory as illustrated by the red lines in those panels. Furthermore, this shift is also topological, in that the shifts vanish for loops that do not enclose the fictitious flux tube. A detailed discussion of the origin and implications of this observation will be presented elsewhere[34].

E. AB inteferometry for a single loop

Our discussions addressed AB inteferometry for setups in which interference patterns are compared following two independent open-loop measurements[35]. In the classical single loop AB setup, an interference pattern is observed at a single screen (point c) as shown in Figure (9). In it, a wavepacket coherently splits at the origin, point a , and propagates toward the mirrors at points b, d respectively, the packets are deflected and allowed to recombine at point c where a measurement is taken. In the calculations described above, and in the adiabatic limit $\Delta/k^2 \gg 1$, we found that (i) the wave packets propagate as a free particle, (ii) in the journey along curve C the packets acquire, in addition to the standard dynamical the phase factor, the phase

$$\exp(i \int_C dr \cdot \mathbf{A}_P). \quad (44)$$

Using Eq. (44) for the paths $a - b - c$ and $a - d - c$ we find that measurements at the screen will be a function of the path integral, along the closed loop,

$$\exp(i \oint dr \cdot \mathbf{A}_P). \quad (45)$$

If that loop encloses the fictitious flux tube then its value is $\exp(i\Phi)$, otherwise it has unit value. Therefore this setup exhibits topological properties consistent with AB theory. In the extreme non-adiabatic limit $\Delta/k^2 \ll 1$ our calculations again demonstrate the validity of properties (i), (ii), with the exception that “free particle” evolution is that of a two-component wavefunction and the phase factor multiplying it is a multi-channel unitary matrix Eq. (42). Therefore, repeating the analysis given

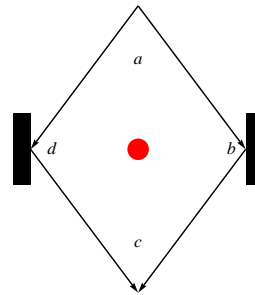


FIG. 9: (Color online) Standard, single loop, AB inteferometry setup. Two coherent packets at origin a split and propagate to the mirrors at points b, d . The mirrors deflect the packets so they recombine at point c where the measurements are made.

above we find measurements at screen c are now proportional to the loop integral

$$P \exp(i \oint dr \cdot \mathbf{A}) = 1. \quad (46)$$

That is, regardless of the loop geometry, topological fringe patterns do not arise and there is no topological AB shift. In summary, our calculations demonstrate that, in the adiabatic limit, solutions generated by the time evolution operator Eq. (16) with the external field configuration Eq.(15) reproduces the standard AB fringe shift. In the limit $\Delta/k \rightarrow 0$, non-adiabatic transitions conspire to wash out topological AB fringes. This conclusion is consistent with that given in Ref. [18]. Nevertheless, we find here that if spin-state dependent measurements are made during traversal of the circuit, topological shifts persist. This counter-intuitive observation will be discussed in more detail elsewhere[34].

III. AB SCATTERING

In the previous section we presented an outline for eliciting AB-like topological effects, for neutral spin 1/2 particles, in an interferometry setup. In standard treatments e.g. [36, 37], the AB effect is discussed in the context of a scattering scenario and so it is instructive to analyze the dynamics generated by Hamiltonian Eq.(16) in this framework. In Ref.[18] a Born-Oppenheimer approximation was used to obtain an equation for the ground state amplitude (in a field theoretic analog of this system), and in which, the vector potential \mathbf{A}_{AB} emerges. Standard time independent methods were applied to demonstrate AB-like scattering. A BO approximation was also used in Ref.[19] in order to suggest that AB-like scattering arises in systems described by Hamiltonian (16).

Here we apply time dependent wave propagation in order to demonstrate AB scattering. However, there are two obstacles that prevent us from simulating pure AB scattering in the Fraunhofer region. The latter requires

propagation of a wave packet from the distant remote past, to the distant future. This is numerically untenable. In addition, the wave packet traverses a region near the origin where singular couplings between the ground and excited adiabatic states arise[34]. We by-pass these difficulties by placing an impenetrable hard-cylinder surrounding the origin and introducing a diagonal counter term $b_{ii}(\mathbf{R}) = \sum_{i \neq j} \mathbf{A}_{ij} \cdot \mathbf{A}_{ji}$, as shown in Eq. (13).

At initial time t_0 we introduce a finite slab-like wave packet shown by the illustration in Figure 10. It proceeds with a mean initial velocity toward the impenetrable cylinder represented in that illustration by the orange colored disk. The wave packet is propagated numerically solving coupled equations (13). The packet mean momentum is chosen so that the inequality $\Delta/k^2 \gg 1$ is satisfied. At a later time t_1 Figure 10 illustrates how the packet diffracts around the cylinder. Subsequently, at t_2 , the forward scattering probability density reaches a detector shown by the red dashed line in that figure.

In Figure 11 we present a high resolution plot for the imaginary part of the wave packet amplitude, at time t_2 , for the two cases where $\Omega = 1/2$ (left panel) and $\Omega = 0$ (right panel) respectively. With $\Omega = 0$ Eqs. (13) decouple, and the ground state amplitude satisfies the free particle Schrodinger equation in the presence of an impenetrable cylinder centered at the origin. The right hand panel of Figure 11 illustrates both the reflected and transmitted components, including interference between the two, of the packet as it is scattered by the cylinder. In the left hand panel we plot the same amplitude except we set the parameter $\Omega = 1/2$ in Eq. (14). It corresponds to the case where $\Phi = \pi$ in Eq. (23). The plot is almost identical to the one obtained for $\Omega = 0$, except for the striking phase dislocation[36], running along a line bisecting the cylinder in the forward scattering direction. This phenomenon is well known in pure AB scattering[36] and, for the case $\Phi = \pi$, is a manifestation of a nodal line for the amplitude along the phase dislocation line. Berry et al.[36] argued that phase dislocation in pure AB scattering, though not a physical observable, is a topological invariant. In Figure (12) we plot the probability amplitude at the observation panel at time t_2 , shown by the line in Fig. (10), for both cases $\Omega = 0$, the blue dashed line, and $\Omega = 1/2$ by the solid red line. Both probability distributions are similar except along the line near $\eta = 0$ in that figure. Both cases exhibit the “shadow” cast in the forward direction by the cylinder, the $\Omega = 0$ plot shows a small enhancement directly “downwind”, at $\eta = 0$, from the cylinder. It corresponds to the 1D analog of the celebrated Poisson spot[38, 39] that occurs when a wavefront diffracts about a circular obstacle. The red line in Fig. (12), which corresponds to the case where $\Phi = \pi$ in AB scattering and which shows a strong suppression of this spot.

Finally, we compare the results shown in Fig. (12) with those obtained in a time independent description. In appendix B, we construct the wave functions used in a standard scattering theory scenario. It obeys boundary

conditions that correspond to an incoming packet in the asymptotic region in the remote past that subsequently scatters off the cylinder. Typically this wave function is used to derive the scattering amplitude in the Fraunhofer region, but here we use it to find the, time independent, probability amplitude at the observation screen shown in Fig. (10). In Figure (12) the dashed blue line represents the case $\Phi = 0$ (i.e. no AB flux tube), and the red line by the $\Phi = \pi$ case. The latter corresponds to maximal AB scattering. As in Fig (12), differences in the probability distributions are most evident near the $\eta \approx 0$ line. Because the incident amplitude extends from $-\infty < \eta < \infty$, Fresnel type interference patterns at larger η manifest here and which are not present in Fig. (12). However, there is qualitative agreement between the two descriptions near the forward direction, in that a strong suppression of the Poisson spot is evident when the AB flux tube has the value $\Phi = \pi$.

In summary we have demonstrated that solutions of Eq. (13) do exhibit the features that arise in standard AB scattering for the collision energy range $\Delta/k^2 \gg 1$.

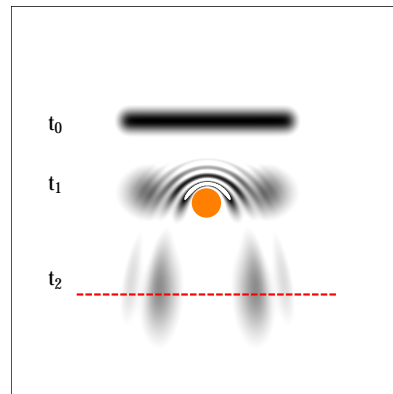


FIG. 10: (Color online) Time series plot of the probability density for an initial wavepacket at t_0 that propagates toward the impenetrable cylinder (orange disk) and is scattered by it. The red dashed line represents a detection screen.

IV. RELATION TO THE MOLECULAR AB EFFECT

A gauge potential equivalent to Eq. (23) (for $\Phi = \pi$) was introduced by Mead and Truhlar [4] in order to describe molecular dynamics near a conical intersection. In this section we explore the relationship between that phenomenon, often called the molecular Aharonov-Bohm (or MAB) effect, and AB-like scattering described in the previous section. It has long been taken for granted, in the molecular physics community, that degeneracy in the form of a conical intersections is an essential requirement for topological effects induced by a vector potential to arise. However, no degeneracy in the physical parameter

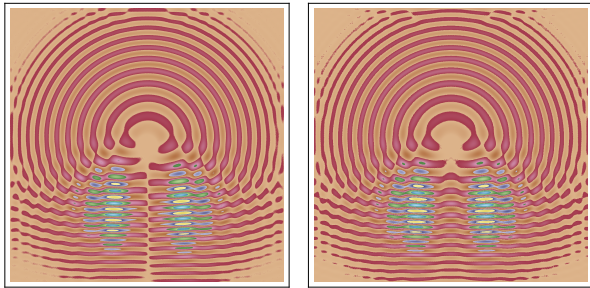


FIG. 11: (Color online) Plots of the imaginary part of the ground state amplitude at time t_2 shown in Figure (10). Right panel corresponds to case $\Phi = 0$, scattering by an impenetrable cylinder. The left panel corresponds to the case $\Phi = \pi$, maximal AB scattering by an impenetrable cylinder.

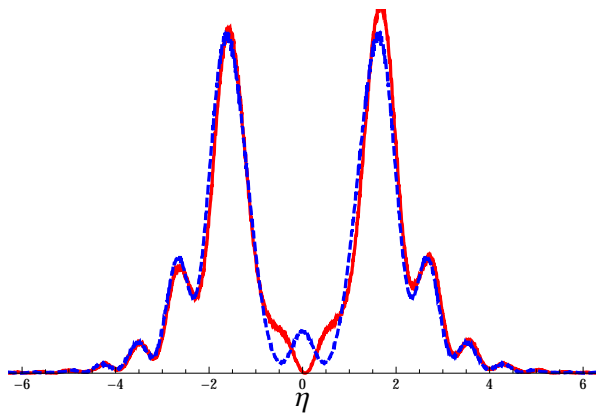


FIG. 12: (Color online) Dashed blue line is a plot of the time dependent probability density, at t_2 and for $\Phi = 0$, along the η axis corresponding to the red dashed line shown in Figure (10). The red solid line corresponds to the case $\Phi = \pi$, maximal AB scattering by an impenetrable cylinder.

space \mathbf{R} is evident in the BO Hamiltonian defined in Eq. (18) as B_0, B_ρ are taken to be constant. This dichotomy presents a certain amount of cognitive dissonance and so deserves closer examination.

Consider a tri-atomic system that possesses a conical intersection at the origin of a parameter space that is spanned by a set of nuclear internal coordinates x, y . Typically they represent various linear combinations of the squares of internuclear distances between the three nuclei[4] in a planar configuration. In this coordinate system the azimuthal angle ϕ is called the pseudorotation and $\rho = \sqrt{x^2 + y^2}$ measures distortions from an equilateral triangle configuration of nuclei. We describe the system by an amplitude $\psi(x, y, \mathbf{r})$ where \mathbf{r} are electronic coordinates. If the electronic, or fast, coordinates are integrated out one can approximate the adiabatic, or electronic, Hamiltonian as a truncated two-dimensional

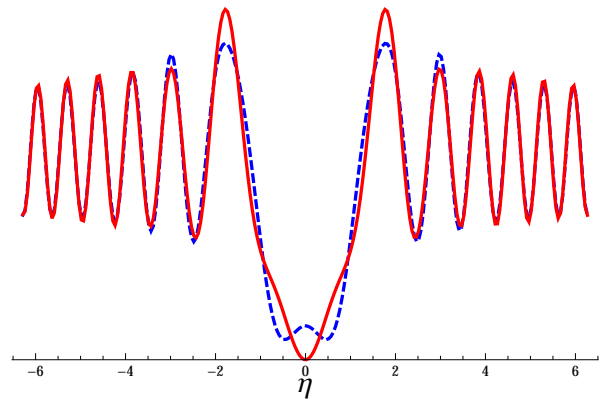


FIG. 13: (Color online) Dashed blue line is a plot of $|\psi|^2$ along the η axis, corresponding to the detection screen shown in figure (10), for solution to Eq. (B1) with $\Phi = 0$. It corresponds to time independent scattering from an impenetrable cylinder at the origin. The red solid line corresponds to the case $\Phi = \pi$, maximal AB scattering by an impenetrable cylinder.

Hilbert space operator, which in the vicinity of the intersection is given by[28]

$$H_{ad} = \begin{pmatrix} x & y \\ y & -x \end{pmatrix}. \quad (47)$$

The eigenvalues of H_{ad} are $\pm\sqrt{x^2 + y^2}$ and correspond to first excited and ground states, respectively, of the electronic Hamiltonian. We approximate the vibronic kinetic energy operator $H_{KE} = -\frac{\hbar^2}{2\mu} \left(\frac{\partial^2}{\partial x^2} + \frac{\partial^2}{\partial y^2} \right)$ where μ is a reduced atomic mass. Therefore,

$$H = -\frac{\hbar^2}{2\mu} \left(\frac{\partial^2}{\partial x^2} + \frac{\partial^2}{\partial y^2} \right) + H_{ad} \quad (48)$$

and has the form given by Eq. (5).

Because H_{ad} is real, Longuet-Higgins and Herzberg[29] constrained its eigenstates to be real-valued and found

$$|\Phi_g\rangle = \begin{pmatrix} -\sin \phi/2 \\ \cos \phi/2 \end{pmatrix} = \tilde{U}(\phi)|g\rangle \\ \tilde{U}(\phi) = \begin{pmatrix} \cos \phi/2 & -\sin \phi/2 \\ \sin \phi/2 & \cos \phi/2 \end{pmatrix} \quad |g\rangle = \begin{pmatrix} 0 \\ 1 \end{pmatrix}, \quad (49)$$

where $|\Phi_g\rangle$ is the ground adiabatic electronic state. They noted that it is multivalued, as its value changes sign in traversing a circuit from $\phi = 0$ to $\phi = 2\pi$. The total system amplitude ψ must be single valued and so in a Born-Oppenheimer approximation in which $\psi = F(x, y)|\Phi_g\rangle$, the vibronic amplitude $F(x, y)$ must undergo a compensating sign change. That argument was used by Mead and Truhlar to invoke the minimal coupling of the vibronic motion, in Eq. (48), with a vector potential given by

$$\mathbf{A}_{MAB} = \frac{\hat{\phi}}{2\rho}. \quad (50)$$

In order to relate this result with the analysis in the previous section we offer a different tack. Instead of constraining the eigenstates of Eq. (47) to be real we do not impose phase restrictions on them[6], but we do require them to be single valued in parameter space x, y . We find that

$$H_{ad} = U_c(\phi)H_{BO}U_c^\dagger(\phi)$$

$$H_{BO} = \begin{pmatrix} \sqrt{x^2 + y^2} & 0 \\ 0 & -\sqrt{x^2 + y^2} \end{pmatrix} \quad (51)$$

where

$$U_c(\phi) = \exp(-i\sigma_2\phi/2) \exp(-i\sigma_3\phi/2) =$$

$$\begin{pmatrix} e^{\frac{i\phi}{2}} \cos\left(\frac{\phi}{2}\right) & -e^{-\frac{i\phi}{2}} \sin\left(\frac{\phi}{2}\right) \\ e^{\frac{i\phi}{2}} \sin\left(\frac{\phi}{2}\right) & e^{-\frac{i\phi}{2}} \cos\left(\frac{\phi}{2}\right) \end{pmatrix}. \quad (52)$$

Unlike the operator $\tilde{U}(\phi)$ given in Eq. (49), which undergoes a sign change as ϕ ranges from 0 to 2π , $U_c(\phi)$ is single valued for all ϕ , excluding the origin, i.e. $U(\phi + 2\pi) = U(\phi)$. Repeating the derivations outlined in the previous sections we arrive at the set of coupled equations for the vibronic amplitudes in the adiabatic picture,

$$-\frac{\hbar^2}{2m} (\nabla - i\mathbf{A})^2 F(\mathbf{R}) + V_{BO}(\mathbf{R})F(\mathbf{R}) = EF(\mathbf{R}). \quad (53)$$

$F(\mathbf{R})$ is a column vector whose entries are the ground and excited state vibronic amplitudes, $V_{BO}(\mathbf{R})$ is the BO eigen-energy matrix and \mathbf{A} is the non-Abelian gauge potential

$$\mathbf{A} = iU_c^\dagger \nabla U_c = \frac{1}{2\rho} \begin{pmatrix} -1 & -i \exp(-i\phi) \\ i \exp(i\phi) & 1 \end{pmatrix}. \quad (54)$$

It is identical to expression (20) for the case $\Omega = 3\pi/2$. This equivalence is a consequence of the fact that $U(\phi)$, and U_c are related, as shown in Appendix C, by a constant unitary matrix. A Born-Oppenheimer projection of Eq. (53) leads to Eq. (8) where \mathbf{A}_P becomes the Mead-Truhlar gauge potential \mathbf{A}_{MAB} .

$U(\mathbf{R})$ defined in Eq. (19) diagonalizes the adiabatic Hamiltonian $\mu_B \boldsymbol{\sigma} \cdot \mathbf{B}$, which for the \mathbf{B} configuration Eq. (15) does not possess degeneracy in \mathbf{R} space. U_c diagonalizes Hamiltonian (47) which exhibits a conical intersection at the origin of \mathbf{R} space. Thus the emergence of the non-trivial gauge structures follow from the properties of the unitary operators that diagonalize the respective adiabatic Hamiltonians, and is insensitive to the fact that H_{BO} may possess degeneracy. In Appendix C we show how both $U(\mathbf{R})$ and U_c can be constructed, via a Wilson line integral, from their respective gauge fields.

Finally, we explore the relationship of this analysis with that given in discussions of Berry's phase[1]. The adiabatic Hamiltonian $H_{ad} = \mu_B \boldsymbol{\sigma} \cdot \mathbf{B}$, given in Eq. (16), shares the structure of Berry's model. In the latter \mathbf{B}

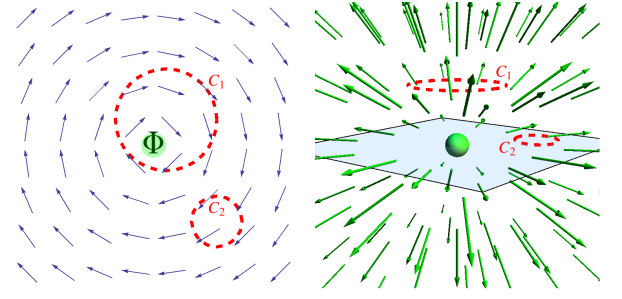


FIG. 14: (Color online). The left panel illustrates the vortex configuration, projected on the xy plane, of the external magnetic field given by Eq. (15), and the red dashed lines are paths in \mathbf{R} space. Φ represents the effective flux tube pointing into the page. The right hand panel shows field lines emanating from the effective Dirac monopole located at the origin. The dashed red lines represent loops in the parameter space of the monopole, and are maps of the corresponding loops in \mathbf{R} space. The blue background plane bisects the monopole.

is taken as a classical parameter that can be arbitrarily varied. Under adiabatic conditions, i.e. slow variation of \mathbf{B} , a spin 1/2 system accrues a phase that is determined by the vector potential, or connection, of a magnetic monopole (see the right panel of Figure 14). The gauge field of the monopole differs from that given in Eq. (23) which describes a magnetic flux tube extended along the z axis. In our discussion \mathbf{B} is a fixed external magnetic field, shown by the vortex lines in the left panel of Figure 14, and gauge field Eqs. (20,23) follows from it by considering variation of parameter \mathbf{R} instead of \mathbf{B} . The gauge structure induced by the former, realized in molecular systems with conical intersections, does not lead to a Lorentz force. However, effective magnetic monopoles in \mathbf{R} space are realized in diatoms[5, 6, 21]. They lead to effective Lorentz forces, (i.e. geometric magnetism), in those systems[6, 21]. In addition, \mathbf{R} is a quantum variable and so true adiabaticity is ill defined. Nevertheless, if we demote \mathbf{R} to a c-number we can consider loops in \mathbf{R} space and relate them to corresponding loops in \mathbf{B} space. This is illustrated in Figure (14). In the left panel of this figure we show a loop C_1 which encloses the flux tube, of magnitude Φ , at the origin. In \mathbf{B} space it corresponds to a loop that subtends a solid angle Ω , from the location of the monopole, so that $\Phi = \pi(1 - \cos \Omega)/2$. A loop C_2 that does not enclose the flux tube corresponds to a loop in \mathbf{B} space that lies in a plane (shown by the blue background in the right panel of that figure) that bisects the monopole.

V. SUMMARY AND DISCUSSION

These examples illustrate how induced geometric phase gauge potentials, that lead to holonomies and effective “magnetic” forces, arise in simple quantum systems without resorting to assumptions that are based on BO - type approximations. We introduced a two-level Hamiltonian which mimics the behavior of a charged particle that is subjected to both electric and magnetic fields in such a way that enable a velocity selector. In another example, that of a neutral spin 1/2 system subjected to an external magnetic field, we showed how AB-like effects arise in low energy solutions to the coupled Schroedinger equations. We introduced and discussed both an interference setup, as well as a scattering scenario, in which such effects arise. In addition we showed how the system transitions from that described by an Abelian gauge potential to that in which non-Abelian effects manifest at higher collision energies.

Dirac[2] noted that if a solution ψ to the Schroedinger equation is multiplied by a phase factor so that $\psi(\mathbf{R}) \rightarrow \psi'(\mathbf{R}) = \exp(i\alpha(\mathbf{R}))\psi(\mathbf{R})$, and since we can always represent $\alpha(\mathbf{R}) = \int_C^{\mathbf{R}} d\mathbf{r} \cdot \mathbf{A}(\mathbf{r})$ this substitution leads to the replacement $\nabla\psi \rightarrow \nabla\psi' - i\mathbf{A}\psi'$. However, conventional quantum mechanics demands that $\psi'(\mathbf{R})$ be single-valued at all \mathbf{R} , and this condition constrains the gauge potential \mathbf{A} to a trivial, pure, gauge which does not lead to new physics. Dirac suggested that minimal coupling of a charged particle with a non-trivial gauge field follows from a non-integrable factor $\alpha(\mathbf{R}, C)$, a functional that depends on the path C . There have been explorations in that direction[40] but difficulties in enforcing single-valuedness has limited the utility of this approach.

The examples provided above illustrate how an aspect of Dirac’s program is realized. Let ψ be a multi-component amplitude and consider the non-Abelian version of Dirac’s substitution, i.e. $\psi \rightarrow \psi' = U(\mathbf{R})\psi$, where $U(\mathbf{R})$ is a single-valued, differentiable unitary matrix operator. In [15] and in Appendix C we showed how $U(\mathbf{R})$ can be expressed as a Wilson line of a non-Abelian, pure, gauge potential \mathbf{A} . Because \mathbf{A} is a pure gauge, issues involving multi-valuedness in $U(\mathbf{R})$ and hence in ψ' do not arise. Nevertheless, as our examples demonstrate, if the gauge symmetry is broken by energy gaps (i.e. non-degeneracy of H_{BO}) non-trivial gauge fields that lead to gauge forces and/or topological holonomies can emerge in low energy solutions to the Schroedinger equation.

Appendix A: Packet dynamics

At lower collision energies, in which the excited Zeeman level is closed, we consider the propagation of a coherent wave packet that is initially localized, as shown in Figure (2). Using the dimensionless coordinates defined in [15], $\xi = x/L, \eta = y/L, \tau = \frac{\hbar}{2mL^2} t$, we take the free

particle wave packet (normalized to the value 2)

$$\begin{aligned} \psi(\xi, \eta, \tau) &= \psi_1(\xi, \eta, \tau) + \psi_2(\xi, \eta, t) \\ \psi_i &= \int \int dk_1 dk_2 \Phi(k_1 - k_{x_i}) \Phi(k_2 - k_{y_i}) \times \\ &\exp(-i\tau(k_1^2 + k_2^2)) \exp(-i\tau\tilde{\Delta}) \times \\ &\exp(ik_1(\xi - \xi_i)) \exp(ik_2(\eta - \eta_i)). \end{aligned} \quad (\text{A1})$$

With the choice

$$\Phi(k) = \frac{\sqrt{a}}{(2\pi^3)^{\frac{1}{4}}} \exp(-a^2 k^2) \quad (\text{A2})$$

$\psi_i(\xi, \eta, \tau)$ is a solution to the equation

$$i\frac{\partial\psi_i}{\partial\tau} = -\frac{\partial^2\psi_i}{\partial\xi^2} - \frac{\partial^2\psi_i}{\partial\eta^2} + \tilde{\Delta}\psi_i \quad (\text{A3})$$

and describes, at $\tau = 0$, a Gaussian wavepacket of width a localized at (ξ_i, η_i) with momenta k_{x_i}, k_{y_i} . $\tilde{\Delta}$ is the energy defect Δ in units of $\frac{2mL^2}{\hbar^2}$. By linearity, the coherent sum $\psi(\xi, \eta, \tau)$ is also a possible packet. Here we chose $\xi_1 = \xi_2 = 0, \eta_1 = -\eta_0, \eta_2 = \eta_0$, and $k_{x_1} = k_{x_2} = k, k_{y_1} = -k_{y_2} = k$. At time $\tau_c = \eta_0/2k$ the two packets coalesce and form the interference pattern illustrated in Figure 2. The center of the merged packets at τ_c passes through the line $\xi = \eta_0$. On it

$$\begin{aligned} \psi(\eta_0, \eta, \tau_c) &= \int \int dk_1 dk_2 \Phi(k_1 - k) \Phi(k_2 - k) \times \\ &\exp(-i\tau_c(k_1^2 + k_2^2)) \exp(ik_1\eta_0) \exp(-i\tau_c\tilde{\Delta}) \times \\ &\left[\exp(ik_2(\eta + \eta_0)) + \exp(-ik_2(\eta - \eta_0)) \right]. \end{aligned} \quad (\text{A4})$$

Integration of Eq. (A4) yields

$$\begin{aligned} |\psi(\eta_0, \eta, \tau_c)|^2 &= \\ &\frac{8a^2 k^2 \exp(-\frac{2a^2 k^2 \eta^2}{4a^4 k^2 + \eta_0^2})}{4a^4 k^2 \pi + \pi \eta_0^2} \cos^2(k\eta). \end{aligned} \quad (\text{A5})$$

Appendix B: AB scattering wave function in the presence of an impenetrable cylinder

Scattering by an impenetrable cylinder, in the presence of a AB flux tube, has been extensively reviewed in the literature [18, 36, 37]. Below we provide an analysis following along lines given in Ref. [36]. We consider the Schroedinger equation,

$$\begin{aligned} (\nabla - i\mathbf{A})^2 \psi + k^2 \psi - U(r)\psi &= 0 \\ \mathbf{A} &= \hat{\phi} \frac{\Phi}{2\pi r} \end{aligned} \quad (\text{B1})$$

where \mathbf{A} is a vector potential, and $U(r)$ is a short range potential, which we take to be that of an impenetrable

cylinder whose axis is perpendicular to the incoming flux. Expressing the wave function

$$\psi(r, \phi) = \sum_{m=-\infty}^{\infty} c_m \exp(im\phi) R_m(r) \quad (\text{B2})$$

we obtain the radial equation,

$$R''(r) + \frac{R'(r)}{r} - \frac{(m-\alpha)^2}{r^2} R(r) + (k^2 - U(r))R(r) = 0 \quad (\text{B3})$$

where $\alpha \equiv \Phi/2\pi$. Its solutions are linear combinations of

$$J_{|m-\alpha|}(kr) \quad N_{|m-\alpha|}(kr).$$

For the repulsive core we require $R(a) = 0$ and therefore the radial solution has the form

$$R(r) = c_1 J_{|m-\alpha|}(kr) + c_2 H_{|m-\alpha|}^{(1)}(kr) \quad (\text{B4})$$

where

$$\frac{c_2}{c_1} = -\frac{J_{|m-\alpha|}(ka)}{H_{|m-\alpha|}^{(1)}(ka)}. \quad (\text{B5})$$

We define the AB amplitude ([27])

$$\psi_{ab}(r, \phi) = \sum_{m=-\infty}^{m=\infty} (-i)^{|m-\alpha|} J_{|m-\alpha|}(kr) \exp(im\phi), \quad (\text{B6})$$

and so choose $c_1 = (-i)^{|m-\alpha|}$. Therefore, according to Eq. (B5)

$$c_2 = -(-i)^{|m-\alpha|} \frac{J_{|m-\alpha|}(ka)}{H_{|m-\alpha|}^{(1)}(ka)}. \quad (\text{B7})$$

and

$$\begin{aligned} \psi(r, \phi) &= \psi_{ab}(r, \phi) - \psi_R(r, \phi) \\ \psi_R(r, \phi) &\equiv \sum_{m=-\infty}^{\infty} -i^{|m-\alpha|} \frac{J_{|m-\alpha|}(ka)}{H_{|m-\alpha|}^{(1)}(ka)} H_{|m-\alpha|}^{(1)}(kr). \end{aligned} \quad (\text{B8})$$

For the value $\alpha = 1/2$, the so called maximal AB scattering case, $\psi_{ab}(r, \phi)$, is given by the closed-form expression [27, 36]

$$\begin{aligned} \psi_{ab}(r, \phi) &= \frac{2}{\sqrt{\pi}} \exp(i\phi/2) \exp(-ikz) \exp(-i\pi/4) \times \\ &\exp(\mp i\pi/4) \text{Erf}(\exp(\mp i3\pi/4) \sqrt{2kr} \cos(\phi/2)) \end{aligned} \quad (\text{B9})$$

where the \pm refers to the regions $0 < \phi \leq \pi$ and $-\pi < \phi \leq 0$ respectively.

Appendix C: Representation of a unitary matrix by a pure gauge field

Consider a unitary matrix $U(\mathbf{R})$ that is continuous, single valued, and has a derivative defined at each point \mathbf{R} , excluding the origin, so that

$$\mathbf{A}(\mathbf{R}) = iU^\dagger(\mathbf{R}) \nabla U(\mathbf{R}) \quad (\text{C1})$$

is a pure gauge potential[3]. Suppose it has the property

$$P \exp(i \oint \mathbf{dR} \cdot \mathbf{A}) = 1 \quad (\text{C2})$$

for any closed path in \mathbf{R} space. Can we then represent $U(\mathbf{R})$ as a Wilson line of the corresponding gauge potential? Here we show that this is the case for the operators $U(\mathbf{R})$ given in Eq.(19), and U_c defined in Eq. (52). We define a path C so that $\mathbf{R}(t) = R_0 \cos(\omega t) \hat{\mathbf{i}} + R_0 \sin(\omega t) \hat{\mathbf{j}}$ on it, and traverses a loop of radius R_0 in the counter-clockwise direction. Consider the (Wilson) line integral along this path from ϕ_0 to ϕ

$$\begin{aligned} W(\phi, \phi_0, C) &= P \exp(i \int_C \mathbf{dR} \cdot \mathbf{A}(\mathbf{R})) \equiv \\ W(t, t_0) &= T \exp(i \int_{t_0}^t A(t)) \end{aligned} \quad (\text{C3})$$

where, $\phi/\omega = t$, $\phi_0/\omega = t_0$, T is the Dyson time-ordering operator,

$$\begin{aligned} A(t) &\equiv \frac{d\mathbf{R}(t)}{dt} \cdot \mathbf{A}(\mathbf{R}(t)) = \\ &\begin{pmatrix} -\omega \sin^2\left(\frac{\Omega}{2}\right) & \frac{1}{2} i e^{-it\omega} \omega \sin(\Omega) \\ -\frac{1}{2} i e^{it\omega} \omega \sin(\Omega) & \omega \sin^2\left(\frac{\Omega}{2}\right) \end{pmatrix} \end{aligned} \quad (\text{C4})$$

and we used Eq. (20). Noting that

$$\frac{dW(t)}{dt} = iA(t)W(t) \quad (\text{C5})$$

we integrate to get

$$W(\phi, \phi_0) = U^\dagger(\phi) U(\phi_0) = \begin{pmatrix} \cos^2\left(\frac{\Omega}{2}\right) + \sin^2\left(\frac{\Omega}{2}\right) e^{-i(\phi-\phi_0)} & -e^{-i\frac{\phi+\phi_0}{2}} \sin\left(\frac{\phi-\phi_0}{2}\right) \sin(\Omega) \\ e^{i\frac{\phi+\phi_0}{2}} \sin\left(\frac{\phi-\phi_0}{2}\right) \sin(\Omega) & \cos^2\left(\frac{\Omega}{2}\right) + \sin^2\left(\frac{\Omega}{2}\right) e^{i(\phi-\phi_0)} \end{pmatrix}. \quad (\text{C6})$$

$W(\phi, \phi_0)$ obeys the group property

$$W(\phi, \phi_0) = W(\phi, \phi_1)W(\phi_1, \phi_0) \quad (\text{C7})$$

for $\phi > \phi_1 > \phi_0$, and since W is unitary we have

$$W^\dagger(t, t_0) = \tilde{T} \exp(-i \int_{t_0}^t A(t)) = \tilde{T} \exp(i \int_{t_0}^t \tilde{A}(t))$$

$$\tilde{A}(t) = \frac{d\tilde{\mathbf{R}}(t)}{dt} \cdot \mathbf{A}(\tilde{\mathbf{R}}(t)) \quad (\text{C8})$$

where \tilde{T} is the anti-time ordering operator, and $\tilde{\mathbf{R}}(t)$ defines a circular path running along the clockwise direction. According to Eq. (C6)

$$U(\phi) = U(\phi_0)W^\dagger(\phi, \phi_0) \quad (\text{C9})$$

where $U(\phi)$ is given in Eq. (19). Therefore we have

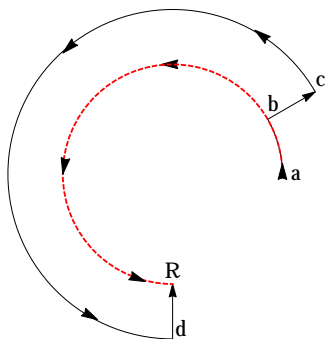


FIG. 15: (Color online). Integration paths for Wilson line integral, where point a lies on a ray $\phi = \phi_0$ and \mathbf{R} lies on the ray ϕ .

shown that $U(\mathbf{R})$ can be defined in terms of a line integral along the path shown by the red dashed arc in Fig. (15). Point a is along the line ϕ_0 (not including the origin) and \mathbf{R} is some arbitrary point (not on the origin). However we can deform the path as shown by the solid line segments in that figure. By the group property Eq. (C7) we can equate

$$W(\mathbf{R}, \phi_0) = W(\mathbf{R}, d)W(d, c)W(c, b)W(b, a) \quad (\text{C10})$$

where we used $W(c, b) = W(\mathbf{R}, d) = 1$, and demonstrate that $U(\mathbf{R})$ can be expressed in terms of the Wilson line, for any right handed path, provided that it does not pass through the origin. We stress, again, such a representation is not possible for the Abelian projection

$$\mathbf{A}_P \equiv \text{Tr} P \mathbf{A} P = \hat{\phi} \frac{1 - \cos \Omega}{2\rho} \quad (\text{C11})$$

as its Wilson loop integral, for any loop surrounding the origin, is not unity. As a consequence

$$U_P \equiv \exp(i \int_C d\mathbf{R} \cdot \mathbf{A}_P)$$

is multivalued. In the same way we also show that operator $U_c(\phi)$, defined in Eq. (52) is given by

$$U_c(\phi) = W^\dagger(\phi, 0) \quad (\text{C12})$$

where we have set $\Omega = 3\pi/2$ in the expression for W . Comparing Eq. (C12), setting $\Omega = 3\pi/2$, with Eq. (C9) we find that

$$U(\phi) = U(0)U_c(\phi)$$

$$U(0) = \exp(3\pi i/2 \sigma_1). \quad (\text{C13})$$

ACKNOWLEDGMENTS

I thank Dr. M. Kiffner, and an anonymous reviewer, for useful comments and suggestions.

-
- [1] M. V. Berry, Proc. R. Soc. Lond. A **392**, 45 (1984).
 - [2] P. A. M. Dirac, Royal Society of London Proceedings Series A **133**, 60 (1931).
 - [3] T. T. Wu and C. N. Yang, Phys. Rev. D **12**, 3845 (1975).
 - [4] C. A. Mead and G. D. Truhlar, The Journal of Chemical Physics **70**, 2284 (1979).
 - [5] J. Moody, A. Shapere, and F. Wilczek, Phys. Rev. Lett. **56**, 893 (1986).
 - [6] B. Zygelman, Phys. Lett. A **125**, 476 (1987).
 - [7] R. Jackiw, Comments At. Mol. Phys. **21** (1988).
 - [8] M. V. Berry, in *Geometric Phases in Physics*, edited by A. Shapere and F. Wilczek (World Scientific Publishing Company, 1989) p. 1.
 - [9] M. V. Berry and J. M. Robbins, Proc. R. Soc. Lond. **A392**, 45 (1992).
 - [10] J. Dalibard, F. Gerbier, G. Juzeliūnas, and P. Öhberg, Reviews of Modern Physics **83**, 1523 (2011).
 - [11] N. Goldman, G. Juzeliūnas, P. Öhberg, and I. B. Spielman, Reports on Progress in Physics **77**, 126401 (2014).
 - [12] G. Juzeliūnas, J. Ruseckas, P. Öhberg, and M. Fleischhauer, Phys. Rev. A. **73**, 025602 (2006).
 - [13] Y. Lin, R. L. Compton, A. R. Perry, W. D. Phillips, J. V. Porto, and I. B. Spielman, Physical Review Letters **102**, 130401 (2009).
 - [14] Y. Lin, R. L. Compton, K. Jiménez-García, J. V. Porto, and I. B. Spielman, Nature **462**, 628 (2009).
 - [15] B. Zygelman, Phys. Rev. A. **86**, 042704 (2012).
 - [16] B. Zygelman, ArXiv e-prints (2012), arXiv:1205.1792 [quant-ph].
 - [17] M. Kiffner, W. Li, and D. Jaksch, Phys. Rev. Lett. **110**, 170402 (2013).
 - [18] J. March-Russell, J. Preskill, and F. Wilczek, Phys. Rev. Lett. **68**, 2567 (1992).

- [19] Y.-I. Shen, Journal of Physics A: Mathematical and General **29**, 913 (1996).
- [20] S. K. Min, A. Abedi, K. S. Kim, and E. K. U. Gross, Phys. Rev. Lett. (2015).
- [21] B. Zygelman, Physical Review Letters **64**, 256 (1990).
- [22] C. A. Mead, Rev. Mod. Phys. **64**, 51 (1992).
- [23] K. Gottfried and T.-M. Yan, *Quantum Mechanics: Fundamentals*, 2nd ed. (Springer, 2003).
- [24] Y. Aharonov, E. Ben-Reuven, S. Popescu, and D. Rohrlich, Phys. Rev. Lett. **65**, 3065 (1990).
- [25] Y. Aharonov and A. Stern, Phys. Rev. Lett. **69**, 3593 (1992).
- [26] A. S. Goldhaber, Phys. Rev. A **71**, 062102 (2005).
- [27] A. Aharonov and D. Bohm, Phys. Rev. **115**, 485 (1959).
- [28] E. Teller, The Journal of Physical Chemistry **41**, 109 (1937).
- [29] G. Herzberg and H. C. Longuet-Higgins, Discuss. Faraday Soc. **35**, 77 (1963).
- [30] If, as in Berry's Hamiltonian, the adiabatic energies are degenerate at an isolated point in a 3-dimensional parameter space, U can be made to be single valued, in a region not including this point, provided that it is defined as two overlapping charts, i.e. $U(\mathbf{R}) = \exp(-i\phi/2\sigma_3) \exp(-i\theta/2\sigma_2) \exp(\pm i\phi/2\sigma_3)$. See also Ref. [21].
- [31] B. Zygelman and A. Dalgarno, Phys. Rev. A **33**, 3853 (1986).
- [32] A. Dalgarno and R. McCarroll, Royal Society of London Proceedings Series A **237**, 383 (1956).
- [33] B. M. and K. Huang, *Dynamical Theory of Crystal Lattices* (Oxford University Press, 1954).
- [34] B. Zygelman, In preparation (2015).
- [35] A. Retzker, Y. Aharonov, A. Botero, S. Nussinov, and B. Reznik, Phys. Rev. A **73**, 032106 (2006).
- [36] M. V. Berry, R. G. Chambers, M. D. Large, C. Upstill, and J. C. Walmsey, Eur. J. Phys. **1**, 154 (1980).
- [37] Y. Aharonov, C. K. Au, E. C. Lerner, and J. Q. Liang, Phys. Rev. D **29**, 2396 (1984).
- [38] S. Nowak, T. Stuhler, Pfau, and J. Mlynek, Phys. Rev. Lett. **81**, 5792 (1998).
- [39] T. Reisinger, A. A. Patel, H. Reingruber, K. Fladischer, W. E. Ernst, G. Bracco, H. I. Smith, and B. Holst, Phys. Rev. A **79**, 053823 (2009).
- [40] S. Mandelstam, Annals of Physics **19**, 1 (1962).